Impeded behavior of an eccentric thermosyphon rotating about a vertical axis

Litong Zhao and G. S. H. Lock
Department of Mechanical Engineering, University of Alberta, Edmonton, Alberta, Canada

Three-dimensional fluid flow and heat transfer in an eccentric thermosyphon rotating about a vertical axis parallel to its own centerline are explored numerically using the SIMPLE-C algorithm under steady, laminar flow conditions. Results have been obtained for Rayleigh numbers up to 10^6 and Ekman numbers down to 2×10^{-3}. The effects of acceleration ratio and eccentricity are discussed. Special attention has been paid to the effect of the Coriolis force on the flow pattern and heat transfer rate.

Keywords: rotating eccentric thermosyphon; impeded flow; numerical analysis

Introduction

Even though the thermosyphon was first suggested for the cooling of high-temperature gas turbine blades over 50 years ago, the literature on rotating thermosyphons is not extensive. In recent years, some attention has been directed towards evaporative systems, the principal aim being the acquisition of empirical data for use in an engineering context. Very little has been written on single-phase behavior. In particular, we know of no theoretical work dealing with natural convection in an eccentric rotating closed tube.

When an eccentric thermosyphon rotates about a vertical axis parallel to its own centerline, the centrifugal force will create a body force field similar to that in a horizontal stationary cavity. Such cavities have been widely studied because of the importance of convection in thermal insulation, metal casting, and crystallization phenomena. The works of Cormack, Leal and Imberger (1974), Cormack, Leal, and Seinfield (1974), and Imberger (1974) provide an appropriate point of departure. These were analytic, numerical, and experimental studies of a two-dimensional (2-D) closed rectangular cavity with the two end walls being held at different temperatures and the side walls being adiabatic. The characteristic flow structure within these slender cavities was revealed: a central bifilamental core region of essentially parallel opposing flows joins two end regions. These findings were supported later by the analysis of Bejan and Tien (1978a, 1978b) using conducting side walls.

Experimental results for the free convective flow of gases in a horizontal cylinder with different end temperatures and a linear temperature distribution along the side wall were reported by Schiroky and Rosenberger (1984) using a laser-Doppler anemometer. It was found that the velocity profiles in the central region near the midlength point were the same as expected from 2-D models, at least for low Rayleigh numbers; for the end regions, pronounced three-dimensional (3-D) flow behavior was observed.

Address reprint requests to Professor Lock at the Department of Mechanical Engineering, University of Alberta, Edmonton, Alberta, Canada T6G 2G8.

Received 13 January 1992; accepted 28 April 1992

Bontoux *et al.* (1986) carried out a more detailed 3-D numerical study of flows in circular cylindrical cavities. They revealed the existence of a paired vortical secondary flow in the midplane.

Recently, Han (1988), Lock and Han (1989), and Lock and Zhao (1992) carried out 3-D numerical studies on buoyant laminar flows in an inclined, square-section cavity. Complete heat transfer curves from the conduction regime to the impeded flow regime were given. It was found that a secondary motion in the form of a vortex pair developed within the core filament in the impeded regime. This secondary flow was found to produce a significant increase in heat transfer rate. When the cavity was inclined to the horizontal position, an annular refluent flow was gradually developed at the end region, and the bifilamental flow was maintained in the central region. The heat transfer rate increased first and then dropped down when the tilt angle increased from 0° to 90°.

The present paper is a numerical study of the flow pattern in a closed, square-section, tubular thermosyphon rotating about a vertical axis parallel to its own axis. The governing equations for steady, laminar flow were first recast in finite-difference form and then solved numerically using a modified version of the SIMPLE algorithm.

Formulation

The geometry and orientation of the thermosyphon is described in Figure 1, which also indicates a Cartesian coordinate system rotating synchronously with the system itself. The thermosyphon is heated from below and cooled at the top. A linear temperature distribution is applied between the two ends. The aspect ratio of the system $A = L/D$ was fixed at 5:1. Under steady, laminar conditions, and using the Boussinesq approximation, the governing equations can be written in component form using the Cartesian coordinate system indicated in Figure 1. Thus,

$$\frac{\partial U}{\partial X} + \frac{\partial V}{\partial Y} + \frac{\partial W}{\partial Z} = 0 \tag{1}$$

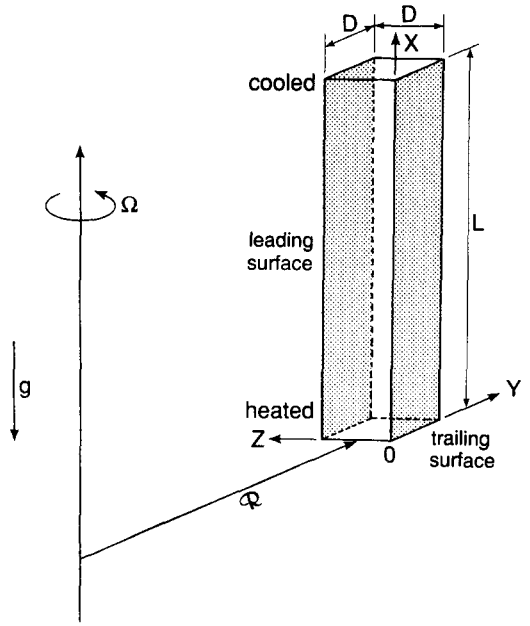

Figure 1 Orientation and coordinate system for a vertical eccentric thermosyphon

$$U\frac{\partial U}{\partial X}+V\frac{\partial U}{\partial Y}+W\frac{\partial U}{\partial Z}=-\frac{1}{\rho}\frac{\partial P}{\partial X}+\nu\left(\frac{\partial^2 U}{\partial X^2}+\frac{\partial^2 U}{\partial Y^2}+\frac{\partial^2 U}{\partial Z^2}\right)+\beta(T-T_0)g \tag{2}$$

$$U\frac{\partial V}{\partial X}+V\frac{\partial V}{\partial Y}+W\frac{\partial V}{\partial Z}=-\frac{1}{\rho}\frac{\partial P}{\partial Y}+\nu\left(\frac{\partial^2 V}{\partial X^2}+\frac{\partial^2 V}{\partial Y^2}+\frac{\partial^2 V}{\partial Z^2}\right)-\beta(T-T_0)\Omega^2(\Re+Y)+2\Omega W \tag{3}$$

$$U\frac{\partial W}{\partial X}+V\frac{\partial W}{\partial Y}+W\frac{\partial W}{\partial Z}=-\frac{1}{\rho}\frac{\partial P}{\partial Z}+\nu\left(\frac{\partial^2 W}{\partial X^2}+\frac{\partial^2 W}{\partial Y^2}+\frac{\partial^2 W}{\partial Z^2}\right)-\beta(T-T_0)\Omega^2\left(Z-\frac{D}{2}\right)-2\Omega V \tag{4}$$

$$U\frac{\partial T}{\partial X}+V\frac{\partial T}{\partial Y}+W\frac{\partial T}{\partial Z}=\kappa\left(\frac{\partial^2 T}{\partial X^2}+\frac{\partial^2 T}{\partial Y^2}+\frac{\partial^2 T}{\partial Z^2}\right) \tag{5}$$

In terms of the nondimensional variables

$$\left.\begin{aligned} x&=\frac{X}{L} \quad y=\frac{Y}{D} \quad z=\frac{Z}{D}\\ u&=\frac{U}{AF} \quad v=\frac{V}{F} \quad w=\frac{W}{F}\\ \phi&=\frac{T-T_0}{T_H-T_0} \quad p=\frac{P}{\rho F^2}\end{aligned}\right\} \tag{6}$$

where

$$F=[\beta(T_H-T_0)\Omega^2(\Re+D)D]^{1/2} \quad \text{and} \quad T_0=(T_H+T_L)/2 \tag{7}$$

the above equations may now be written in nondimensionalized form as follows:

$$\frac{\partial u}{\partial x}+\frac{\partial v}{\partial y}+\frac{\partial w}{\partial x}=0 \tag{8}$$

$$u\frac{\partial u}{\partial X}+v\frac{\partial u}{\partial y}+w\frac{\partial u}{\partial z}=-\frac{1}{A^2}\frac{\partial p}{\partial x}+\left(\frac{2\mathrm{Pr}}{\mathrm{Ra}}\right)^{1/2}\left[\frac{1}{A^2}\frac{\partial^2 u}{\partial x^2}+\frac{\partial^2 u}{\partial y^2}+\frac{\partial^2 u}{\partial z^2}\right]+\frac{1}{AR_g}\phi \tag{9}$$

$$u\frac{\partial v}{\partial x}+v\frac{\partial v}{\partial y}+w\frac{\partial v}{\partial z}=-\frac{\partial p}{\partial y}+\left(\frac{2\mathrm{Pr}}{\mathrm{Ra}}\right)^{1/2}\left[\frac{1}{A^2}\frac{\partial^2 v}{\partial x^2}+\frac{\partial^2 v}{\partial y^2}+\frac{\partial^2 v}{\partial z^2}\right]-\left(\frac{R_1+y}{R_1+1}\right)\phi+\left(\frac{2\mathrm{Pr}}{\mathrm{Ra\,Ek}^2}\right)^{1/2}w \tag{10}$$

Notation

A	Surface area, aspect ratio
D	Length in the Y- and Z-directions
Ek	Ekman number
g	Gravitational acceleration
k	Thermal conductivity
L	Length in X-direction
Nu	Nusselt number
$P(p)$	Absolute (nondimensional) pressure
Pr	Prandtl number
Q	Total heat flux through the system
Ra	Rayleigh number
R_g	Acceleration ratio
R_l	Length ratio
$\Re$	Distance from the axis of rotation to the tube inner surface
T	Temperature
$U(u)$	Velocity (nondimensional) in the X-direction
$V(v)$	Velocity (nondimensional) in the Y-direction
$W(w)$	Velocity (nondimensional) in the Z-direction
$X(x)$	Coordinate (nondimensional)
$Y(y)$	Coordinate (nondimensional)
$Z(z)$	Coordinate (nondimensional)

Greek symbols

β	Thermal expansion coefficient
κ	Thermal diffusivity
ν	Dynamic viscosity
ρ	Density
ϕ	Normalized temperature
Ω	Rotating speed

Subscripts

0	Reference state
H	High temperature
L	Low temperature

Superscript

c	Characteristic scale

Table 1 The effect of mesh size on Nusselt number

	Grid	Nu	ΔNu/Nu (%)
FPS-164			
Scientific Computer	51 × 15 × 15	2.3019	—
IBM Risc 6000	77 × 23 × 23	2.2746	−1.2
	51 × 23 × 23	2.3043	0.1
	51 × 15 × 15	2.3686	2.9
	45 × 15 × 15	2.4364	5.8
	41 × 15 × 15	2.4542	6.6
	51 × 13 × 13	2.4886	8.1

Note: Ra = 5×10^4, Ek = 2×10^{-3}, $R_g = 100$, $R_l = 100$

$$u\frac{\partial w}{\partial x} + v\frac{\partial w}{\partial y} + w\frac{\partial w}{\partial z} = -\frac{\partial p}{\partial z} + \left(\frac{2\mathrm{Pr}}{\mathrm{Ra}}\right)^{1/2}\left[\frac{1}{A^2}\frac{\partial^2 w}{\partial x^2} + \frac{\partial^2 w}{\partial y^2} + \frac{\partial^2 w}{\partial z^2}\right] - \left(\frac{z-0.5}{R_l+1}\right)\phi - 2\left(\frac{2\mathrm{Pr}}{\mathrm{Ra\,Ek}^2}\right)^{1/2} v \quad (11)$$

$$u\frac{\partial \phi}{\partial x} + v\frac{\partial \phi}{\partial y} + w\frac{\partial \phi}{\partial z} = \left(\frac{2}{\mathrm{Pr\,Ra}}\right)^{1/2}\left[\frac{1}{A^2}\frac{\partial^2 \phi}{\partial x^2} + \frac{\partial^2 \phi}{\partial y^2} + \frac{\partial^2 \phi}{\partial z^2}\right] \quad (12)$$

where $\mathrm{Ra} = \beta(T_H - T_L)\Omega^2(\Re + D)D^3/\nu\kappa$ is the diameter-based Rayleigh number, $\mathrm{Ek} = \nu/\Omega D^2$ is the Ekman number, $\mathrm{Pr} = \nu/\kappa$ is the Prandtl number, fixed at 100 to represent a viscous liquid, $R_g = \Omega^2(\Re + D)/g$ is the acceleration ratio, and $R_l = \Re/D$ is the eccentricity. Including the aspect ratio, six parameters emerge. Four of these—Ra, Ek, R_g and R_l—will be studied in detail.

The hydrodynamic boundary conditions are

$u = v = w = 0$, at $x = 0$, $x = 1$, $y = 0$, $y = 1$, $z = 0$, $z = 1$

while the thermal boundary conditions are

$\phi = 1$, at $x = 0$

$\phi = -1$, at $x = 1$

$\phi = 1 - 2x$, at $y = 0$, $y = 1$, $z = 0$, $z = 1$

The above equations were solved numerically using the algorithm of Patankar (1980) in the SIMPLE-C version suggested by Van Doormaal and Raithby (1984). A uniform 51 × 15 × 15 mesh network was used to generate field data. Convergence of the solutions was accepted if the average residual and the successive relative errors in the dependent variables were both within 1%.

The Nusselt number to be determined as a function of the system parameters was defined by

$$\mathrm{Nu} = \frac{QL}{Ak(T_H - T_L)} \quad (13)$$

where Q is the total heat transfer rate supplied through all the walls of the tube and the area A is chosen as half of the total wall area of the tube, i.e., $A = D^2 + 2LD$.

Since there appear to be no experimental or analytical results that can be used for direct comparison, it is not possible to confirm the present solutions independently. However, the program has been tested against the results presented by Mallinson and de Vahl Davis (1977); differences in the Nusselt number and maximum velocity were less than 2 percent. The uniqueness of the data was tested by using different input. Except where otherwise noted, the initial conditions had no noticeable effect on the final result.

For further validation, the results in this paper, which were obtained on an FPS-164 Scientific Computer, were subjected to a grid test conducted on an IBM Risc 6000 Computer using different mesh sizes. All the meshes tested were equally good at describing the flow structure. A comparison of Nusselt numbers calculated from different mesh sizes is given in Table 1. Also, heat transfer rates into and out of the system were calculated for all the data in this paper, the difference being within 2 percent. It is therefore suggested that the accuracy in the Nusselt number using the 51 × 15 × 15 grid system is about ±5 percent. The ability of this mesh to capture flow behavior has been established previously (see Bontoux *et al.* 1986; Lock and Zhao 1992; Lock and Han 1989; Schiroky and Rosenberger 1984).

Results and discussion

The effect of the Rayleigh number

Overall Nusselt number as a function of Rayleigh number is given in Figure 2. The shape and magnitudes shown are similar to those of the stationary horizontal thermosyphon (see Han 1988; Lock and Zhao 1992; Lock and Han 1989), with the definition of Ra modified by replacing $\Omega^2(\Re + D)$ with g. This suggests that the eccentric and horizontal thermosyphons have similar regime behavior. For Rayleigh numbers less than $10^{2.5}$, heat is transferred mainly by conduction, even though convection occurs theoretically as long as there is a temperature difference between the two ends. From the definition of the Nusselt number, Nu → 1/11 as Ra → 0. Above $\mathrm{Ra} = 10^{2.5}$, convection gradually becomes more important and heat transfer increases significantly. As indicated by Lock and Han (1989), a boundary-layer flow regime begins at about Ra-10^7 for this aspect ratio ($A = 5$). The range in which Ra is larger than $10^{2.5}$ and smaller than 10^6 is appropriately described as an impeded regime. It is this regime that is the subject of this paper.

The impeded regime, unlike the boundary-layer regime, is characterized by viscous effects propagating throughout the entire tube cross section (Lock 1992). Under these conditions, the slope of the Nu ~ Ra curve is 1.0, theoretically (Lock 1992). In Figure 2, a slope of about 0.9 occurs in the range of Ra from 10^4 to 10^5. In the left half of the impeded regime, a concave curve joins the conduction regime; in the right half, a convex curve joins the boundary-layer regime. The impeded regime thus acts like an extended transition between the conduction and boundary-layer regimes.

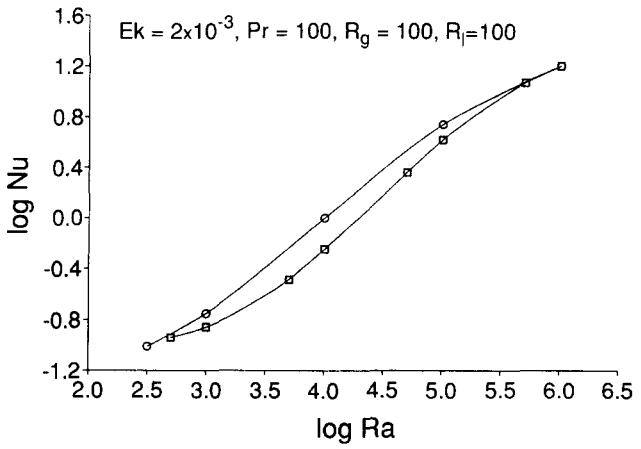

Figure 2 Effect of Rayleigh number on heat transfer in an eccentric thermosyphon. ○ = numerical data from Lock and Han (1989)

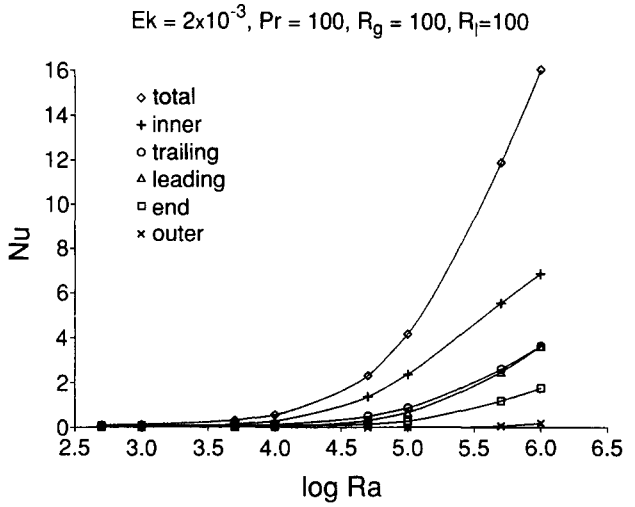

Figure 3 Components of the heat transfer rate

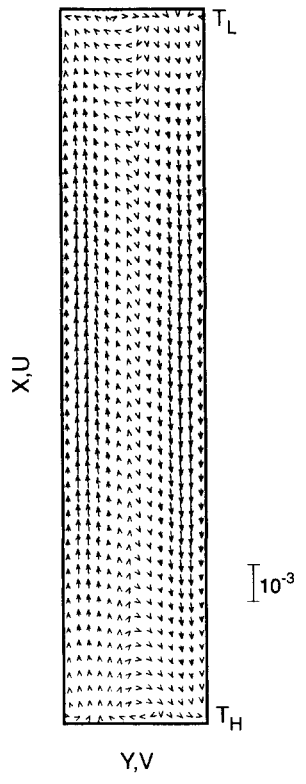

Figure 4 Primary velocity field in plane $z = 0.46$: Ra = 5×10^4

The details of heat transfer from each face are shown in Figure 3. The distribution and variations are similar to those of the horizontal stationary thermosyphon (Han 1988; Lock and Han 1989). Evidently, most of the heat addition takes place on the leading, trailing, and inner surfaces.

The basic flow pattern in a stationary horizontal thermosyphon consists of a simple primary loop upon which is superimposed a secondary circulation induced by lateral temperature gradients. Figure 4 illustrates the primary (X-direction) flow of the corresponding eccentric thermosyphon at Ra = 5×10^4. In the midlength region, the familiar two-filament flow is evident, but near the two ends the flow is more complicated. Figures 5 and 6 show the main flow profile and the secondary flow, respectively. At the hot (lower) end, under the influence of the direct buoyancy force, as in stationary horizontal thermosyphon, the fluid in a lateral plane will flow in the Y-direction to complete the main flow cycle. Under the influence of the Coriolis force, however, the flow in the Y-direction will induce a flow in the Z-direction. Since these two forces act together, the secondary flow is changed to the present S-shape. As seen in Figure 6, it is a clockwise vortical motion in the upper part, and an anticlockwise vortical motion in the lower part. Away from the ends, the Coriolis effect becomes weaker. At the midlength plane, two pairs of weak vortices, both induced by the lateral (radial) temperature gradients, were found. Over the length of the tube, these must become reconciled with the S-pattern in the end regions.

Referring to the governing equations (Equations 9 to 11), if the Ekman number is fixed, when the Rayleigh number decreases the magnitude of the Coriolis term will increase relative to the buoyancy force. Hence, for smaller Rayleigh numbers, a stronger Coriolis effect will result; and for larger Rayleigh numbers, the opposite will be true. The primary circulation and the main flow profile at Ra = 5×10^3 are the same as for Ra = 5×10^4, except they are weaker. Figure 7 shows the corresponding secondary flow field. Near the hot end, the secondary flow is the same as for Ra = 5×10^4 in Figure 6. With the Coriolis force relatively stronger, the end flow is propagated further towards the midlength plane. The two pairs of vortices found in Figure 6 are too weak to appear in Figure 7.

With Ra = 10^6, the primary circulation, the main flow profile, and the secondary flow field are shown in Figures 8, 9, and 10, respectively. For such a high Rayleigh number, the Coriolis force is weaker relative to the buoyancy force. As a

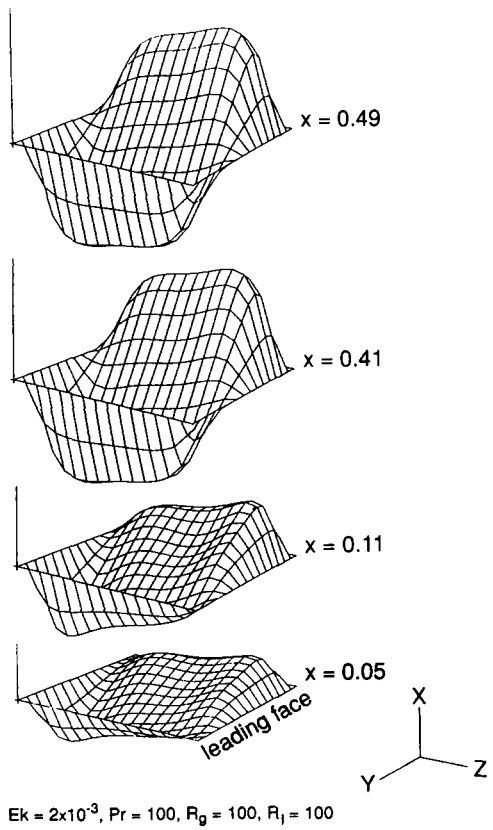

Figure 5 Development of the primary velocity profile: Ra = 5×10^4

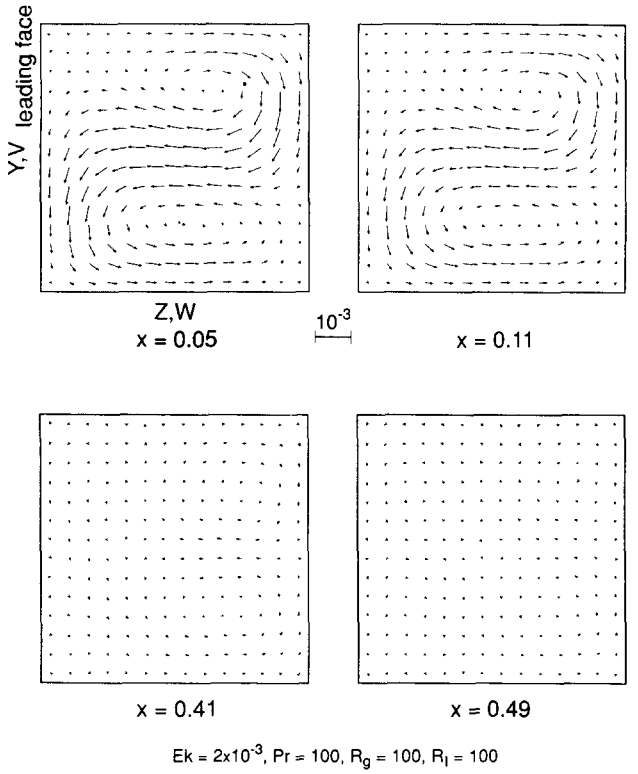

Figure 6 Development of the transverse velocity field: Ra = 5×10^4

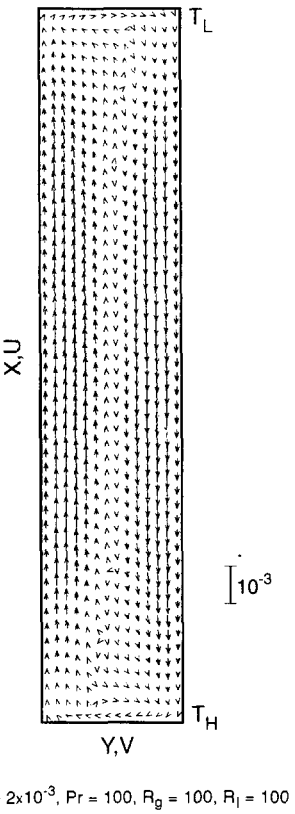

Figure 8 Primary velocity field in plane $z = 0.46$: Ra = 10^6

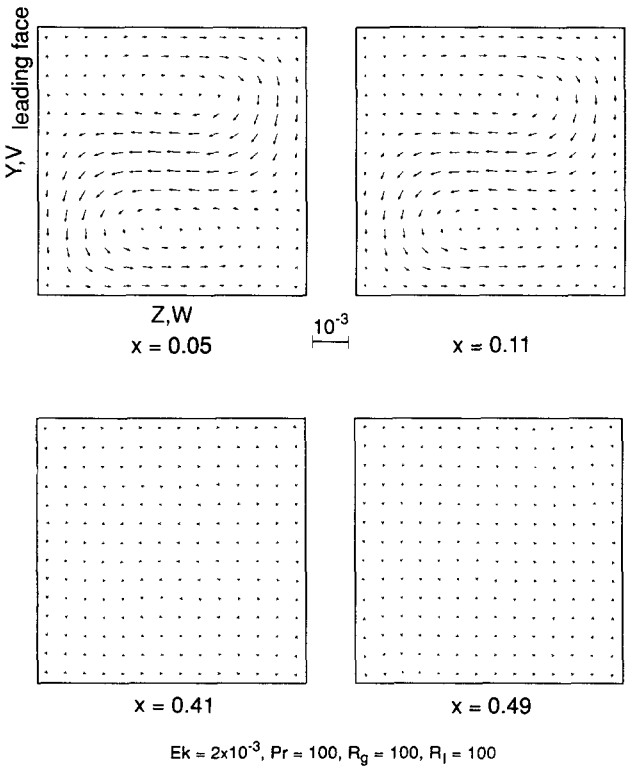

Figure 7 Development of the transverse velocity field: Ra = 5×10^3

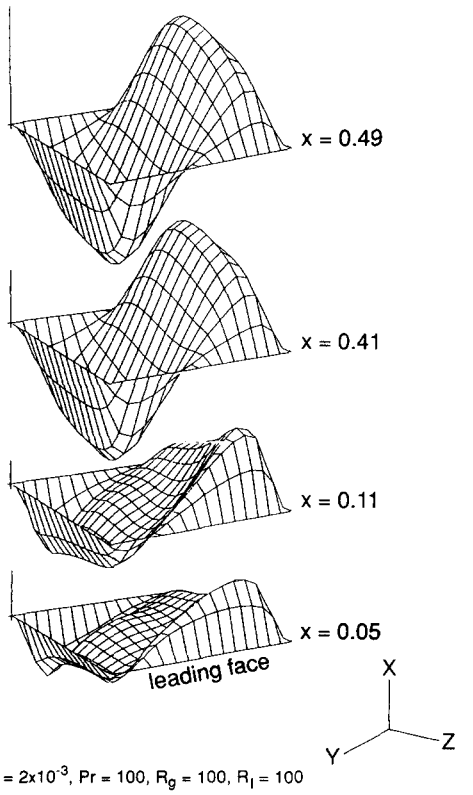

Figure 9 Development of the primary velocity profile: Ra = 10^6

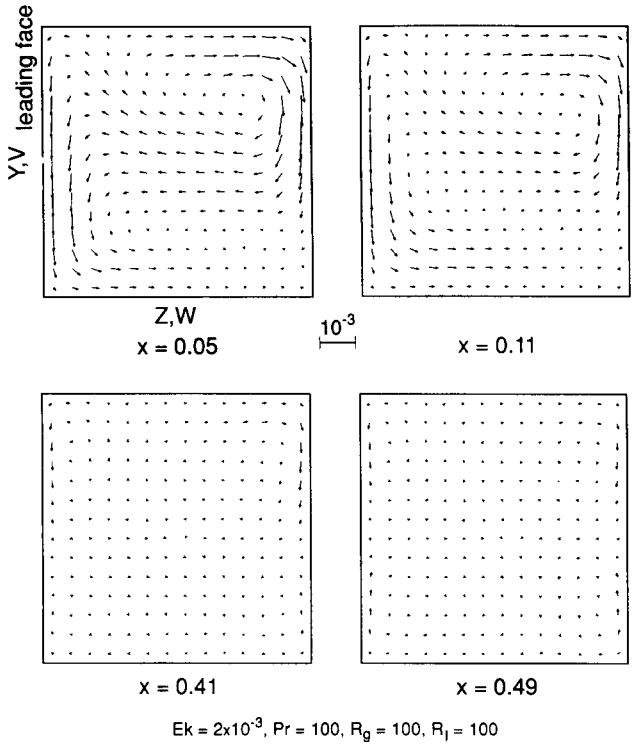

Figure 10 Development of the transverse velocity field: Ra = 10^6

result, the secondary flow in the end region is closer to that found in the stationary horizontal thermosyphon (Lock and Han 1984). The two pairs of vortices in the midlength region are correspondingly stronger. The twist of the main flow profile near the ends is restricted to near the side wall.

The effect of the Ekman number

The Ekman number, representing the relative importance of viscous and Coriolis effects, is always of major interest in the study of rotating systems. For higher Ekman numbers, meaning a smaller Coriolis effect, the system will behave more like a stationary system.

With other parameters constant (Ra = 5×10^4, Pr = 100), the flow pattern with Ek = 2×10^{-3} has been presented above. For a higher Ekman number, Ek = 5×10^{-2}, the primary flow circulation, the main flow profile, and the secondary flow field are shown in Figures 11, 12, and 13, respectively. The primary circulation is again a single cell. Near the end, the secondary flow is only slightly modified by the Coriolis force at the center of the tube. This modification is reflected in the main flow profile; the flow is slightly twisted and is stronger than at Ek = 2×10^{-3}. In the midlength region of the thermosyphon, a bifilamental main flow is again present, and two pairs of vortices induced by lateral temperature gradients are formed.

The individual-surface heat transfer rates as functions of Ekman number are plotted in Figure 14. For Ekman numbers from 10^{-1} to 10^{-2}, the overall heat transfer rate decreases only slightly. Below Ek = 10^{-2}, however, the heat transfer rate drops more quickly. This appears to be because, as Ek decreases and the Coriolis effect increases, the secondary flow near the end is twisted more to an S-shape; the direct buoyancy force is then balanced more closely by the Coriolis force. As a result, the main flow velocity is retarded and the heat transfer rate drops.

The effect of Coriolis force on the heat transfer rate may be estimated from a scaling analysis of Equations 1 to 5. A balance of the principal terms, the pressure gradient, and the largest viscous force, in the X-direction momentum equation gives

$$0 = -\frac{1}{\rho}\frac{\partial P}{\partial X} + \nu\frac{\partial^2 U}{\partial Y^2} \tag{14}$$

In the Y-direction, the balance of Coriolis force, buoyancy force, and pressure gradient gives

$$-2\Omega W = -\frac{1}{\rho}\frac{\partial P}{\partial Y} - \beta(T - T_0)\Omega^2\Re \tag{15}$$

which, like Equation 14, may be justified a posteriori. Eliminating the pressure,

$$2\Omega\frac{\partial W}{\partial X} = \nu\frac{\partial^3 U}{\partial Y^3} + \beta\Omega^2\Re\frac{\partial T}{\partial X} \tag{16}$$

When the Coriolis force balances the direct (radial) buoyancy force, as suggested by the flow profile, Equation 16 reveals that

$$\frac{2\Omega W^c}{\beta\Omega^2\Re T^c} = 0(1) \tag{17}$$

where the superscript c indicates the corresponding scale of the variable: $T^c = 0(T_H - T_L)$.

Likewise, a balance of the principal terms in the energy equation gives

$$U\frac{\partial T}{\partial X} + V\frac{\partial T}{\partial Y} + W\frac{\partial T}{\partial Z} = \kappa\frac{\partial^2 T}{\partial Y^2} \tag{18}$$

Hence, when radial conduction is balanced by lateral, Coriolis-generated advection, Equation 18 reveals

$$\frac{W^c(Y^c)^2}{\kappa Z^c} = 0(1) \tag{19}$$

where $Z^c = 0(D)$.

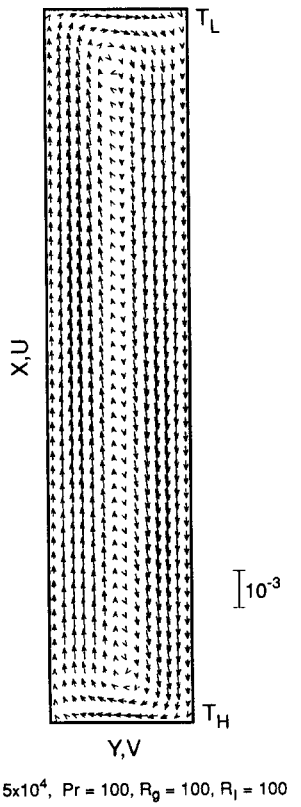

Figure 11 Primary velocity field in plane $z = 0.46$: Ek = 2×10^{-2}

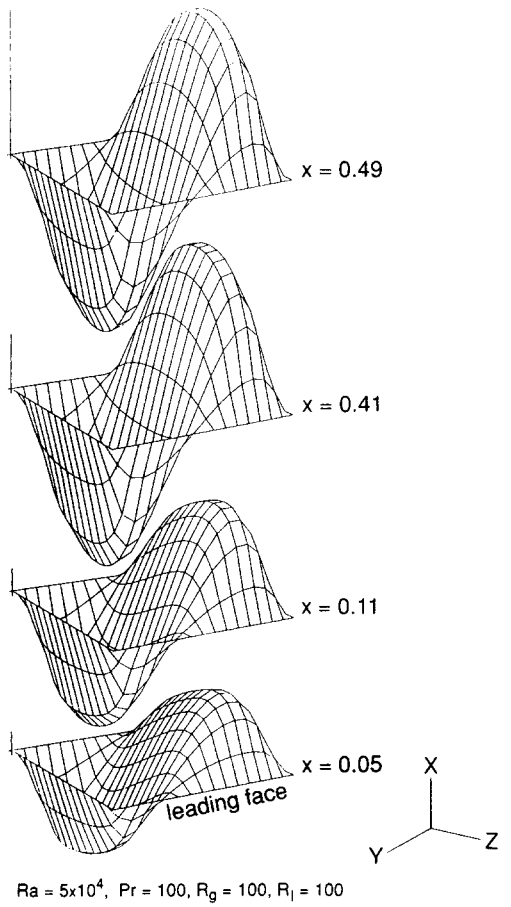

Figure 12 Development of the primary velocity profile: $\mathrm{Ek} = 2 \times 10^{-2}$

Using Equations 17 and 19,

$$W^c = \frac{\beta\Omega^2\Re T^c}{2\Omega} = \frac{\kappa}{2D}\mathrm{EkRa}$$

where

$$\mathrm{Ra} = \beta T^c\Omega^2\Re D^3/\nu\kappa, \qquad \mathrm{Ek} = \nu/\Omega D^2$$

and

$$(Y^c)^2 = \frac{\kappa D}{W^c}$$

or

$$Y^c = D\left(\frac{2}{\mathrm{Ek\ Ra}}\right)^{0.5}$$

The heat transfer rate attributable to this Coriolis-driven advection may now be estimated from

$$Q = qLD = 0(\rho C_p T^c L W^c Y^c)$$

Hence

$$\mathrm{Nu} = \frac{qD}{kT^c} = 0\left(\frac{\mathrm{Ek\ Ra}}{2}\right)^{0.5} \qquad (20)$$

The asymptote provided by Equation 20 is plotted in Figure 14. It seems that the above analysis is an accurate representation of the essential physics in the lower reaches of the impeded regime, where $\mathrm{Nu} \propto \mathrm{Ra}^{0.5}$. The largest neglected terms in Equations 14, 15, and 18 are about 1 percent of those retained. Behavior thus corresponds to a Coriolis-impeded regime in which the heat transfer rate decreases as the Ekman number decreases. It is quite possible that for even lower Ekman numbers the end flows may become unstable and break into cells; the Coriolis-impeded regime would then be succeeded by a new regime in which heat transfer rates could rise substantially. The truth of this speculation must await further study.

The effect of the acceleration ratio

As the acceleration ratio $R_g = \Omega^2(\Re + D)/g$ decreases, gravity becomes more important. Gravity introduces a body force field

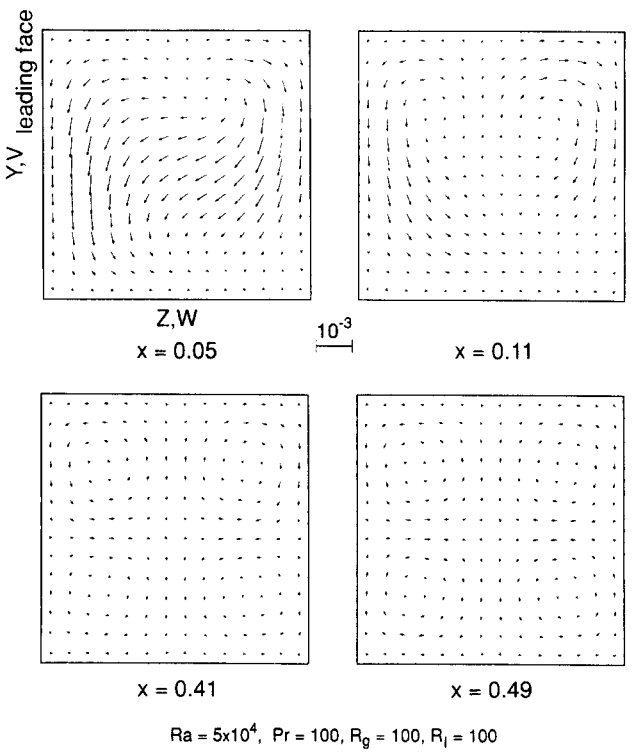

Figure 13 Development of the transverse velocity field: $\mathrm{Ek} = 2 \times 10^{-2}$

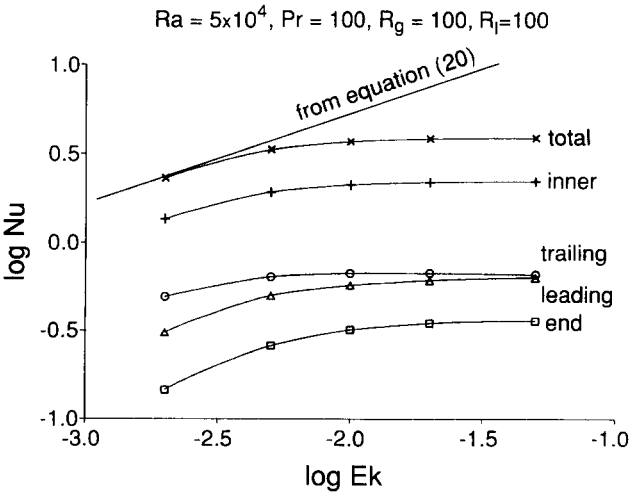

Figure 14 Effect of Ekman number on heat transfer

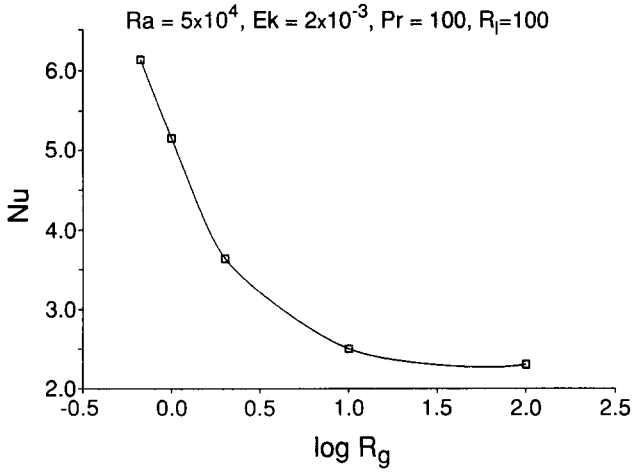

Figure 15 Effect of acceleration ratio on heat transfer

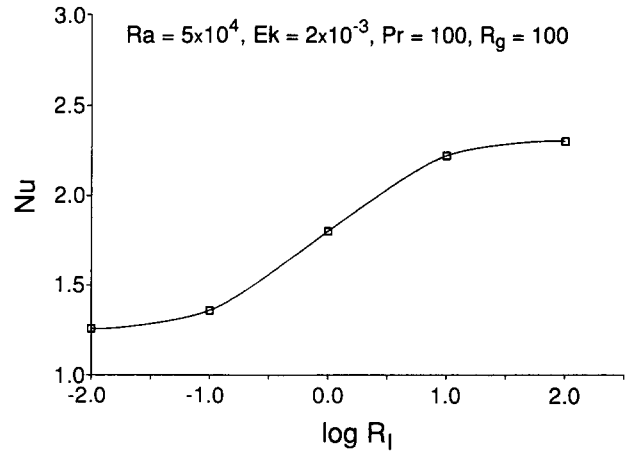

Figure 16 Effect of eccentricity on heat transfer

that is in the opposite direction to the temperature gradient for the arrangement being considered. The system is thus under the action of both direct and indirect buoyancy forces. The effect of acceleration ratio on Nusselt number is shown in Figure 15.

For R_g from 100 down to 10, it is evident that the heat transfer rate changes very little. This suggests that as long as R_g is larger than 10, gravity can be neglected without any serious error in calculating the Nusselt number. When R_g decreases from 10 to 1, the Nusselt number increases substantially.

At $R_g = 1$, with other parameters constant ($Ra = 5 \times 10^4$, $Ek = 2 \times 10^{-3}$, and $R_I = 100$), the flow pattern is similar to that at $R_g = 100$. In the main circulation, a tendency towards annular refluent flow appears near the ends. This is clearly due to the direct gravitational buoyancy force.

The effect of eccentricity

The effect of eccentricity on Nusselt number is shown in Figure 16. For R_I larger than 10, it was found that the centrifugal force in the Y-direction can be treated as uniform, and the component of the centrifugal force in the Z-direction can be neglected. The flow pattern is the same. The Nusselt number is the same. For R_I less than 10, the heat transfer rate decreases gradually. The Nusselt number drops from 2.22 at $R_I = 10$ to 1.26 at $R_I = 0$.

As R_I decreases, the centrifugal force field also decreases. It also has an increasing component in the Z-direction, but this has little effect on the flow pattern. Even at $R_I = 0$, when the inner surface coincides with the axis of rotation, the flow pattern is almost the same as at $R_I = 100$, except it is weaker.

Conclusions

In this paper, the flow pattern and heat transfer characteristics of the rotating eccentric thermosyphon were explored numerically under laminar, steady conditions.

With the thermosyphon rotating about a vertical axis parallel to its centerline, the centrifugal force creates a body force field similar to that in a horizontal stationary thermosyphon. The body force field is perpendicular to the main temperature gradient; the system is therefore driven by indirect buoyancy force, except near the ends. A bifilamental main circulation was formed, with the cooler fluid moving down at the outer surface and the hotter fluid moving up at the inner surface. Near the closed ends, under the influence of both the buoyancy force and the Coriolis force, an S-shape secondary flow appeared; this secondary flow modified the main flow profile.

The curve of Nusselt number against Rayleigh number was similar to that for a stationary horizontal thermosyphon in both magnitude and shape. Flow patterns were similar for all Rayleigh numbers.

For higher Ekman numbers, indicating a smaller Coriolis effect, the flow pattern was closer to that of a stationary system, and the flow was stronger. For relatively low Ekman numbers, direct buoyancy forces near the end came into a closer balance with the Coriolis force. As a result, the main flow velocity was retarded, and the heat transfer rate decreased.

With a reduced acceleration ratio R_g, gravity becomes more important. An annular refluent flow was detected near the ends as the result of the gravity-induced buoyancy force. When $R_g = 0(1)$, the heat transfer rate was then found to increase.

The change of eccentricity had little effect on the flow pattern. A lower heat transfer rate accompanied a decrease in R_I.

Acknowledgment

This work was supported by the Natural Sciences and Engineering Council of Canada to whom we are grateful.

References

Bejan, A. and Tien, C. L. 1978a. Laminar natural convection heat transfer in a horizontal cavity with different end temperatures. *Trans. ASME C: J. Heat Transfer*, **100**, 641

Bejan, A. and Tien, C. L. 1978b. Fully developed natural counterflow in a long horizontal pipe with different end temperatures. *Int. J. Heat Mass Transfer*, **21**, 701

Bontoux, P., Smutek, C., Roux, B. and Lacroix, J. M. 1986. Three-dimensional buoyancy-driven flows in cylindrical cavities with differentially heated endwalls. Part 1. Horizontal cylinders. *J. Fluid Mech.*, **169**, 211

Cormack, D. E., Leal, L. G. and Imberger, J. 1974. Natural convection in a shallow cavity with differentially heated endwalls. Part 1: Asymptotic theory. *J. Fluid Mech.*, **65**, 209

Cormack, D. E., Leal, L. G. and Seinfield, J. N. 1974. Natural

convection in a shallow cavity with differentially heated endwalls. Part 2: Numerical solutions. *J. Fluid Mech.*, **65**, 231

Han, Jianchiu. 1988. Orientational effects in a buoyant cavity flow. M.Sc. thesis, Dept. of Mechanical Engineering, University of Alberta, Edmonton

Imberger, J. 1974. Natural convection in a shallow cavity with differentially heated endwalls. Part 3: Experimental results. *J. Fluid Mech.*, **65**, 247

Lock, G. S. H. and Zhao, Litong. 1992. Natural convection in honeycomb wall spaces. *Int. J. Heat Mass Transfer*, **35** (1), 155

Lock, G. S. H. and Han, J.-C. 1989. Buoyant laminar flow of air in a long, square-section cavity aligned with the ambient temperature gradient. *J. Fluid Mech.*, **207**, 489

Lock, G. S. H. 1992. *The Tubular Thermosyphon*. Oxford University Press, Oxford

Mallinson, G. D. and de Vahl Davis, G. 1977. Three-dimensional natural convection in a box: a numerical study. *J. Fluid Mech.*, **83**, 1

Patankar, S. V. 1980. *Numerical Heat Transfer and Fluid Flow*. McGraw-Hill, New York

Schiroky, G. H. and Rosenberger, F. 1984. Free convection of gases in a horizontal cylinder with differentially heated end walls. *Int. J. Heat Mass Transfer*, **27**, 587

Van Doormaal, J. P. and Raithby, G. D. 1984. Enhancements of the SIMPLE method for predicting incompressible fluid flows. *Numer. Heat Transfer*, **7**, 147